First Measurement of the Muon Neutrino Interaction Cross Section and Flux as a Function of Energy at the LHC with FASER

FASER Collaboration

Roshan Mammen Abraham,[1] Xiaocong Ai,[2] John Anders,[3] Claire Antel,[4] Akitaka Ariga,[5,6] Tomoko Ariga,[7] Jeremy Atkinson,[5] Florian U. Bernlochner,[8] Tobias Boeckh,[8] Jamie Boyd,[3] Lydia Brenner,[9] Angela Burger,[3] Franck Cadoux,[4] Roberto Cardella,[4] David W. Casper,[1] Charlotte Cavanagh,[10] Xin Chen,[11] Dhruv Chouhan,[8] Andrea Coccaro,[12] Stephane Débieux,[4] Monica DÓnofrio,[13] Ansh Desai,[14] Sergey Dmitrievsky,[15] Radu Dobre,[16] Sinead Eley,[13] Yannick Favre,[4] Deion Fellers,[14] Jonathan L. Feng,[1] Carlo Alberto Fenoglio,[4] Didier Ferrere,[4] Max Fieg,[1] Wissal Filali,[8] Elena Firu,[16] Edward Galantay,[3,4] Ali Garabaglu,[17] Stephen Gibson,[18] Sergio Gonzalez-Sevilla,[4] Yuri Gornushkin,[15] Carl Gwilliam,[13] Daiki Hayakawa,[6] Michael Holzbock,[3] Shih-Chieh Hsu,[17] Zhen Hu,[11] Giuseppe Iacobucci,[4] Tomohiro Inada,[7] Luca Iodice,[4] Sune Jakobsen,[3] Hans Joos,[3,19] Enrique Kajomovitz,[20] Hiroaki Kawahara,[7] Alex Keyken,[18] Felix Kling,[21] Daniela Köck,[14] Pantelis Kontaxakis,[4] Umut Kose,[10] Rafaella Kotitsa,[3] Susanne Kuehn,[3] Thanushan Kugathasan,[4] Lorne Levinson,[22] Ke Li,[17] Jinfeng Liu,[11] Yi Liu,[2] Margaret S. Lutz,[3] Jack MacDonald,[23] Chiara Magliocca,[4] Toni Mäkelä,[1] Lawson McCoy,[1] Josh McFayden,[24] Andrea Pizarro Medina,[4] Matteo Milanesio,[4] Théo Moretti,[4] Mitsuhiro Nakamura,[25] Toshiyuki Nakano,[25] Laurie Nevay,[3] Ken Ohashi,[5] Hidetoshi Otono,[7] Hao Pang,[11] Lorenzo Paolozzi,[4,3] Pawan Pawan,[13] Brian Petersen,[3] Titi Preda,[16] Markus Prim,[8] Michaela Queitsch-Maitland,[26] Hiroki Rokujo,[25] André Rubbia,[10] Jorge Sabater-Iglesias,[4] Osamu Sato,[25] Paola Scampoli,[5,27] Kristof Schmieden,[23] Matthias Schott,[23] Anna Sfyrla,[4] Davide Sgalaberna,[10] Mansoora Shamim,[3] Savannah Shively,[1] Yosuke Takubo,[28] Noshin Tarannum,[4] Ondrej Theiner,[4] Eric Torrence,[14] Oscar Ivan Valdes Martinez,[26] Svetlana Vasina,[15] Benedikt Vormwald,[3] Di Wang,[11] Yuxiao Wang,[11] Eli Welch,[1] Monika Wielers,[29] Yue Xu,[17] Samuel Zahorec,[3,30] Stefano Zambito,[4] and Shunliang Zhang[11]

[1] *Department of Physics and Astronomy, University of California, Irvine, CA 92697-4575, USA*
[2] *School of Physics, Zhengzhou University, Zhengzhou 450001, China*
[3] *CERN, CH-1211 Geneva 23, Switzerland*
[4] *Département de Physique Nucléaire et Corpusculaire, University of Geneva, CH-1211 Geneva 4, Switzerland*
[5] *Albert Einstein Center for Fundamental Physics, Laboratory for High Energy Physics, University of Bern, Sidlerstrasse 5, CH-3012 Bern, Switzerland*
[6] *Department of Physics, Chiba University, 1-33 Yayoi-cho Inage-ku, 263-8522 Chiba, Japan*
[7] *Kyushu University, Nishi-ku, 819-0395 Fukuoka, Japan*
[8] *Universität Bonn, Regina-Pacis-Weg 3, D-53113 Bonn, Germany*
[9] *Nikhef National Institute for Subatomic Physics, Science Park 105, 1098 XG Amsterdam, Netherlands*
[10] *Institute for Particle Physics, ETH Zürich, Zürich 8093, Switzerland*
[11] *Department of Physics, Tsinghua University, Beijing, China*
[12] *INFN Sezione di Genova, Via Dodecaneso, 33–16146, Genova, Italy*
[13] *University of Liverpool, Liverpool L69 3BX, United Kingdom*
[14] *University of Oregon, Eugene, OR 97403, USA*
[15] *Affiliated with an international laboratory covered by a cooperation agreement with CERN.*
[16] *Institute of Space Science - INFLPR Subsidiary, Bucharest, Romania*
[17] *Department of Physics, University of Washington, PO Box 351560, Seattle, WA 98195-1460, USA*
[18] *Royal Holloway, University of London, Egham, TW20 0EX, United Kingdom*
[19] *II. Physikalisches Institut, Universität Göttingen, Göttingen, Germany*
[20] *Department of Physics and Astronomy, Technion—Israel Institute of Technology, Haifa 32000, Israel*
[21] *Deutsches Elektronen-Synchrotron DESY, Notkestr. 85, 22607 Hamburg, Germany*
[22] *Department of Particle Physics and Astrophysics, Weizmann Institute of Science, Rehovot 76100, Israel*
[23] *Institut für Physik, Universität Mainz, Mainz, Germany*
[24] *Department of Physics & Astronomy, University of Sussex, Sussex House, Falmer, Brighton, BN1 9RH, United Kingdom*
[25] *Nagoya University, Furo-cho, Chikusa-ku, Nagoya 464-8602, Japan*
[26] *University of Manchester, School of Physics and Astronomy, Schuster Building, Oxford Rd, Manchester M13 9PL, United Kingdom*

[27] *Dipartimento di Fisica "Ettore Pancini", Università di Napoli Federico II, Complesso Universitario di Monte S. Angelo, I-80126 Napoli, Italy*
[28] *National Institute of Technology (KOSEN), Niihama College, 7-1, Yakumo-cho Niihama, 792-0805 Ehime, Japan*
[29] *Particle Physics Department, STFC Rutherford Appleton Laboratory, Harwell Campus, Didcot, OX11 0QX, United Kingdom*
[30] *Charles University, Faculty of Mathematics and Physics, Prague, Czech Republic*

(Dated: May 7, 2025)

This letter presents the measurement of the energy-dependent neutrino-nucleon cross section in tungsten and the differential flux of muon neutrinos and anti-neutrinos. The analysis is performed using proton-proton collision data at a center-of-mass energy of 13.6 TeV and corresponding to an integrated luminosity of $(65.6 \pm 1.4)\,\mathrm{fb}^{-1}$. Using the active electronic components of the FASER detector, 338.1 ± 21.0 charged current muon neutrino interaction events are identified, with backgrounds from other processes subtracted. We unfold the neutrino events into a fiducial volume corresponding to the sensitive regions of the FASER detector and interpret the results in two ways: We use the expected neutrino flux to measure the cross section, and we use the predicted cross section to measure the neutrino flux. Both results are presented in six bins of neutrino energy, achieving the first differential measurement in the TeV range. The observed distributions align with Standard Model predictions. Using this differential data, we extract the contributions of neutrinos from pion and kaon decays.

Introduction The Large Hadron Collider (LHC) produces an intense beam of neutrinos in the forward direction, originating from the decay of pions, kaons, and charmed hadrons from proton-proton (pp) collisions. The precision study of these neutrinos will carry broad implications for investigating neutrino properties, quantum chromodynamics, astroparticle physics, and exploring phenomena beyond the Standard Model [1, 2]. In particular, they provide an opportunity to measure the neutrino interaction cross section in a previously unexplored energy range spanning from 360 GeV to 6.3 TeV, bridging the gap between fixed-target measurements [3] and astroparticle data [4]. Studying collider neutrinos was originally suggested in 1984 [5], but these neutrinos have only been measured recently, since they are outside of the instrumented acceptance of typical LHC experiments. In spring 2023, the FASER Collaboration directly observed collider neutrinos for the first time [6]. This observation was shortly after confirmed by the SND@LHC Collaboration [7]. Neutrino interaction cross sections at TeV energies were measured for the first time using the FASER emulsion detector [8]. These measurements mark collectively the dawn of collider neutrino physics [9]. In this letter, we report the first measurement of the charged current (CC) interaction cross section and the differential flux of muon neutrinos and anti-neutrinos as a function of the neutrino energy. The analysis uses pp collision data recorded by the FASER detector and corresponding to an integrated luminosity of $(65.6 \pm 1.4)\,\mathrm{fb}^{-1}$ collected at a center-of-mass energy of 13.6 TeV.

The FASER Detector The FASER detector is located in the TI12 tunnel, approximately 480 m downstream of the ATLAS interaction point (IP1) and is aligned with the beam collision axis line-of-sight (LOS). Due to the pp crossing angle in IP1, the LOS is shifted downward by about 6.5 cm with respect to the center of the detector[1]. The detector is shielded from the ATLAS IP by about 100 m of rock and concrete. Most background particles are thus either absorbed or are deflected by the LHC magnets, whereas weakly interacting neutrinos are unaffected.

The detector is briefly described below, with a more detailed overview provided in Ref. [10]. FASER consists of a FASERν emulsion neutrino detector, the VetoNu, Veto, Timing and Pre-shower scintillator stations, a tracking spectrometer including three 0.57 T dipole magnets, and an electromagnetic calorimeter. The active transverse area of the detector is defined by the 200 mm diameter magnet aperture. The FASERν emulsion detector consists of 730 layers of interleaved tungsten plates and emulsion films. It has a width of 25 cm, a height of 30 cm and a total mass of 1.1 metric tons. In this analysis, FASERν serves only as the target for neutrino interactions and the electronic detector components are used to identify the neutrino events. The VetoNu scintillator station is positioned in front of the neutrino target in order to veto any incoming charged particles. It consists of two modules measuring 30 cm × 35 cm, which is significantly larger than the target and therefore allows charged particles entering with an angle with respect to the LOS

[1] The pp half-crossing angle in IP1 was −160 µrad for 2022 data taking and varied between −165 µrad and −135 µrad for 2023 data taking resulting in slightly different LOS positions.

to also be discarded. The other scintillator stations are positioned after the neutrino target and are used for triggering and timing measurements. The Veto scintillator station is located after the FASERν emulsion detector and before the first magnet, the Timing station is positioned between the first and second magnets, and the Pre-shower station is located after the last magnet and in front of the calorimeter. Events can be triggered by signals from the scintillator stations and calorimeter, with a typical trigger rate of about 1 kHz [11]. The tracking system consists of an interface tracking station (IFT) and three tracking spectrometer stations [12]. Each tracking station is constructed from three planes comprising eight double-sided ATLAS semiconductor tracker (SCT) barrel modules [13] per plane.

Dataset and Simulated Samples This analysis uses data obtained during runs with stable beam conditions collected in 2022 and 2023. These periods correspond to a total integrated luminosity of $(65.6 \pm 1.4)\,\text{fb}^{-1}$ [14–16] after data quality selection. To study the detector response to neutrino interactions, 2.8×10^6 charged and neutral current (NC) neutrino interactions corresponding to an integrated luminosity of $10\,\text{ab}^{-1}$ were simulated. The neutrino fluxes were obtained using the fast neutrino flux simulation of Ref. [17] and adjusted to match the LHC Run 3 configuration [18]. `EPOS-LHC` [19] is used to simulate the production of light hadrons, and the predictions from `POWHEG` [20–22] and `PYTHIA 8.3` [23] are employed to model charmed hadron production [24]. The interaction of neutrinos with the detector is simulated using the `GENIE 3.04.0` [25–27] event generator. All other particle interactions in the FASER detector are simulated using `GEANT4` [28], with the `FTFP_BERT` physics list as the default. FASER's offline software system is based on the Athena software from the ATLAS Collaboration [29] and the ACTS software framework [30] is used for the reconstruction of charged particle tracks.

Selection and Background Rejection The analysis is optimized to select CC muon neutrino interactions within the fiducial volume, which produce a high-momentum muon traversing the entire detector. The fiducial volume is defined as a cylinder with a diameter of 200 mm around the central axis of the tracking spectrometer, closely resembling the experimental setup. The analysis selections and background estimates were finalized prior to examining data in the signal region to prevent bias. Events are selected if triggered by any scintillator downstream of the VetoNu scintillators, which operate with full efficiency for muons. A colliding bunch crossing at the ATLAS interaction point is required to exclude beam backgrounds and cosmic muons. We use the measured charge in the VetoNu scintillator station to discard charged background events. Neutrino interactions in the target can produce a charge in the VetoNu scintillator predominantly from low-energy neutrons produced through the de-excitation of tungsten nuclei. Thus, we additionally use the time difference between the VetoNu scintillators in front of the target and the Veto scintillators after the target to identify neutrino interactions. For background events, this time difference corresponds to the muon's time of flight. In contrast, neutrino interactions produce charge in the two scintillator stations from different particles, typically leading to larger time differences. This is exploited by defining a reduced charge as the measured charge in each VetoNu scintillator, integrated over the time window expected for a background muon to deposit energy. The reduced charge closely matches the total scintillator charge for muons but is typically much smaller for neutrinos. We require it to be less than 30 pC, ensuring high signal efficiency while rejecting almost all background events. We also require scintillator signals compatible with a muon in all downstream scintillator layers. We require at least one track that passes through all three tracking stations of the FASER spectrometer. For events with multiple tracks the one with the highest momentum is assumed to originate from the muon and is used to determine the neutrino energy. A large number of secondary particles can be produced in neutrino interactions, which can saturate the IFT tracking station located directly after the FASERν emulsion detector. As a result, only the three tracking spectrometer stations are used for track reconstruction. To exclude events with tracks that do not traverse the full spectrometer or have poor quality, tracks are required to have at least 14 hits in the silicon tracker across at least seven layers[2] and to possess a reasonable fit quality. The tracks are reconstructed starting from the most downstream tracking station in order to increase the efficiency for selecting CC neutrino interactions, which can have a large number of hits in the upstream tracking stations. To reduce the contribution from background events, the track is required to have momentum greater than 100 GeV. It is extrapolated to estimate its position at the Veto and VetoNu scintillator stations. We require that the track must lie within 95 mm from the central axis of the detector in all tracking stations, including the IFT, and within 120 mm at the VetoNu scintillator station. Finally, we require that the angle of the track with respect to the detector axis is less than 25 mrad. These radial and angular cuts suppress incoming charged particles that enter FASER at large radii or angles. With these selections we expect to observe almost exclusively CC muon neutrino and anti-neutrino interactions.

Background Estimation The primary source of backgrounds arises from high-momentum muons, originating upstream of FASER. Almost all of these are vetoed by the VetoNu scintillators. The inefficiencies of the two layers were measured to be smaller than 10^{-7} per layer

[2] A good track passing through all tracking stations typically has 18 silicon hits across nine layers

using events which pass the event selection but have a reduced charge larger than 30 pC in one of the two layers. Assuming that the two scintillator layers are independent, we expect for the recorded luminosity about 10^{-6} muons going undetected through both layers, which is negligible compared to the other backgrounds. Muons incident at a large radius and low momentum can geometrically evade the VetoNu scintillator station but may still create a signal-like track in the detector. The expected yield is estimated from data using a sideband containing tracks that pass the event selection but have a momentum smaller than 100 GeV. As the contribution from neutrinos is non-negligible in the higher momentum bins of the sideband, we subtract the expected neutrino yields from the data. We then fit the track momentum distribution in the range of 10 GeV to 100 GeV and extrapolate to our signal region. The extrapolation is performed separately for positively and negatively charged tracks to estimate the background in charge and momentum bins. The resulting number of geometric background (Geo. bgr.) events is compatible with zero in all bins. More details on the geometric background are given in appendix A. Muons may also interact with material upstream of the detector and produce secondary neutral hadrons that can enter the FASER detector and produce tracks. We estimate the contribution of the neutral hadron background by using simulations corresponding to about $2\,\mathrm{ab}^{-1}$ of integrated luminosity within a radial distance of 150 mm. A large fraction of these events fail the event selection, either because the parent muon, which generated the neutral hadron, hits the VetoNu scintillator and fails the reduced VetoNu charge cut, or because the neutral hadron interacts and is fully absorbed in the 8 interaction lengths of the FASERν emulsion detector, without leaving any track through the detector. With this, the expected number of neutral hadron events, passing the event selection, is less than 10^{-3} events for the studied integrated luminosity, and is therefore considered negligible. The backgrounds from cosmic rays and LHC beam background have been studied using events occurring when there are no collisions, and are found to be negligible. In addition to the signal neutrino interactions, identified as CC muon neutrino interactions in the fiducial volume (ν_μ CC fid.), there are a small number of electron neutrino (ν_e CC) or tau neutrino interactions (ν_τ CC), interactions outside of the fiducial volume (ν_μ CC non-fid.), and neutral current neutrino interactions (ν NC) that pass the event selection. We estimate the contribution of these neutrino interactions from simulation and subtract them from data. The resulting number of events is listed in Table I.

Signal Extraction We apply a linear scaling to the reconstructed muon momentum, such that $p'_\mu = p_\mu/0.8$. The factor of 0.8 describes that muons passing the event selection typically retain, on average, 80 % of the incident neutrino energy and results in a more diagonal response matrix, and therefore smaller uncertainties on the unfolded number of neutrino interactions. We define six bins in the ratio of the muon unit charge q and calibrated muon momentum, q/p'_μ, with bin edges

$$\left[-\frac{1}{100}, -\frac{1}{300}, -\frac{1}{600}, -\frac{1}{1000}, \frac{1}{1000}, \frac{1}{300}, \frac{1}{100}\right] \mathrm{GeV}^{-1}\,.$$

This binning results in a comparable expected number of events in each bin, and separates muons originating from neutrinos and anti-neutrinos up to a momentum of 1 TeV. The charge identification accuracy is significantly reduced above this threshold, and we thus combine muons and anti-muons with a larger momentum into a single bin.

We unfold the number of reconstructed muons (n^i_μ) to the number of neutrino interactions in the fiducial volume (n^k_ν) within bins of the ratio of the negative lepton number[3] and neutrino energy, $-L/E_\nu$, via

$$n^i_\mu = \sum_k M_{ik}\,\epsilon_k\,n^k_\nu + n^i_{\mathrm{bkg}}\,, \tag{1}$$

with M_{ik} denoting the response matrix, which relates the reconstructed, calibrated muon momentum in q/p'_μ bin i to the neutrino energy in $-L/E_\nu$ bin k (c.f. appendix B). Further, ϵ_k denotes the efficiency of neutrino events to be reconstructed within the fiducial volume, and n^i_{bkg} are the estimated backgrounds from geometric muons and non-signal neutrino interactions, which includes ν_μ CC interactions outside of the fiducial volume.

The response matrix and efficiency are obtained from simulation and systematic uncertainties are implemented with nuisance parameters. The number of neutrino interactions is determined through a binned extended maximum likelihood fit, expressed as:

$$\mathcal{L} = \prod_i^{\mathrm{bins}} \mathcal{P}(N^i_\mu | n^i_\mu) \times \prod_l \mathcal{G}_l\,, \tag{2}$$

where $\mathcal{P}$ represents a Poisson distribution with N^i_μ as the number of observed events and n^i_μ as the number of expected events (calculated using Eq. 1) in bin i of q/p'_μ. The term $\mathcal{G}_l$ corresponds to Gaussian priors constraining nuisance parameters from source l. The likelihood function in Eq. 2 is numerically minimized using the `iminuit` package [31].

Using the simulated neutrino flux, we calculate the energy-dependent neutrino-nucleon interaction cross section σ^k from the unfolded and efficiency corrected yields

[3] Note that the negative lepton number $-L$ of the neutrino is equal to the unit charge q of the muon produced in the CC neutrino interaction.

TABLE I. Number of simulated signal and background, and observed events for an integrated luminosity of $65.6\,\mathrm{fb}^{-1}$ for the six q/p'_μ bins, with q denoting the muon unit charge and p'_μ the calibrated muon momentum. The uncertainty on the simulated number of neutrino interactions is dominated by the flux uncertainty.

	$q/p'_\mu[\mathrm{GeV}^{-1}]$	$[\frac{-1}{100}, \frac{-1}{300}]$	$[\frac{-1}{300}, \frac{-1}{600}]$	$[\frac{-1}{600}, \frac{-1}{1000}]$	$[\frac{-1}{1000}, \frac{1}{1000}]$	$[\frac{1}{1000}, \frac{1}{300}]$	$[\frac{1}{300}, \frac{1}{100}]$	Total
				Simulation				
Signal	ν_μ CC (fid.)	33.6± 7.6	59.5± 9.1	51.6± 8.8	84.1±21.4	50.1±11.4	19.6± 5.9	298.4±42.6
Bgr.	ν_μ CC (non-fid.)	3.6± 1.4	3.7± 1.7	2.3± 1.3	2.0± 1.2	2.6± 1.3	2.9± 1.3	17.1± 6.6
	ν_e CC	0.7± 0.5	0.2± 0.2	0.1± 0.1	0.1± 0.2	0.4± 0.5	0.9± 0.7	2.3± 1.9
	ν_τ CC	0.0± 0.1	0.0± 0.1	0.0± 0.1	0.0± 0.0	0.1± 0.1	0.0± 0.1	0.2± 0.4
	ν NC	1.4± 0.5	0.4± 0.4	0.1± 0.2	0.1± 0.2	0.6± 0.4	1.3± 0.8	4.0± 1.4
	Geo. bgr.	0.2± 0.6	0.0± 0.1	0.0± 0.0	0.0± 0.0	0.0± 0.0	0.0± 0.0	0.3± 0.6
	Total	39.5± 9.2	63.9±10.2	54.1± 9.6	86.3±22.3	53.7±12.1	24.7± 7.5	322.3±50.5
				Data				
	Total	50	97	71	69	48	27	362

for each $-L/E_\nu$ bin k, via

$$\sigma^k = \frac{n_\nu^k}{\rho_A \cdot \mathrm{L} \cdot \iint j_{\mathrm{sim}}^k \,\mathrm{d}E\mathrm{d}A}\,, \tag{3}$$

where $\iint j_{\mathrm{sim}}^k \,\mathrm{d}E\mathrm{d}A$ denotes the simulated neutrino flux density j_{sim} integrated over the cross sectional area of the fiducial volume A and the neutrino energy of a given bin E in units of number of neutrinos per integrated luminosity, $\rho_A = (1.022 \pm 0.010) \times 10^{27}\,\mathrm{nucleon/cm}^2$ is the area nucleon density and $\mathrm{L} = (65.6 \pm 1.4)\,\mathrm{fb}^{-1}$ is the integrated luminosity.

Conversely, assuming the theoretical cross section, the total flux ϕ^k through the fiducial volume in each neutrino energy bin k is determined via

$$\phi^k = \frac{n_\nu^k}{\rho_A \cdot \mathrm{L} \cdot \sigma_{\mathrm{sim}}^k}\,. \tag{4}$$

Since the neutrino cross section varies within a measured bin, we use the flux-weighted cross section σ_{sim} within a bin. This depends on how the flux varies in each energy bin, and we apply a systematic uncertainty related to the variation using the different generators considered. Additionally, we follow the approach in Ref. [18] and apply a 6 % uncertainty to account for the difference between cross section predictions of the Bodek-Yang model [32–34] and more recent models [35, 36].

Systematic Uncertainties The presented results are affected by several systematic uncertainties. To estimate the uncertainty from the modeling of the neutrino interactions and the passage of the particles, produced in the neutrino interaction, through the detector, we run `GENIE` and `GEANT4` with different tunes and physics lists modifying the final state interactions and hadron transport. More details on these models are given in appendix C. To quantify a systematic uncertainty due to mismodeling of detector components or responses in the simulation, we vary the nominal selection requirements within a range determined by comparisons between data and simulation. In particular, the positions of the SCT modules in the tracking stations can deviate from their nominal positions, resulting in a different momentum scale and resolution between simulation and data. Following a similar approach to that used in Ref. [37], we study the impact of these misalignments on our analysis using simulations with misaligned geometries that reproduce the performance observed in data. The systematic uncertainty on the number of background geometric muon events originates from the statistical uncertainties on the data and the uncertainty on the simulated number of neutrinos in the $p_\mu < 100\,\mathrm{GeV}$ region. The uncertainty on the number of non-signal neutrino interactions is estimated from simulation and dominated by the flux uncertainty. To estimate the uncertainty from neutrino flux predictions, we follow Ref. [18] and simulate neutrino interactions using the flux from the MC generators described in appendix C. The neutrino rate and energy distribution depend on the distance from the LOS, which is determined by the beam crossing angle at the IP. We simulate neutrino interactions for half-crossing angles of both $-160\,\mu\mathrm{rad}$ and $-135\,\mu\mathrm{rad}$ and apply the difference as a systematic uncertainty for all time periods where the crossing angle was not $-160\,\mu\mathrm{rad}$ (26.9 % of all events). Fig. 1 summarizes the resulting relative systematic uncertainties on the determined number of fiducial neutrino interactions in bins of the neutrino energy.

Results After subtracting the number of expected background events, we observe

$$n_{\nu,\mathrm{obs}} = 338.1 \pm 19.0\,(\mathrm{stat.}) \pm 8.8\,(\mathrm{sys.}) \tag{5}$$

events from CC muon neutrino and anti-neutrino interactions. This agrees well with the expected value of 298.4 ± 42.6 within the uncertainties. Table I and Fig. 2 (top panel) show the number of observed and expected signal events in each bin. We observe more negatively charged muons with an energy between 300 GeV and

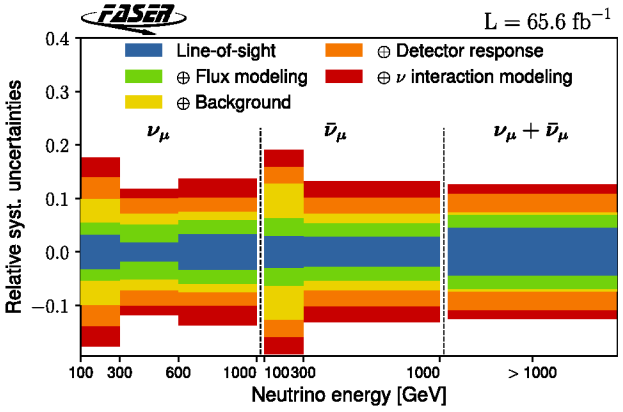

FIG. 1. The relative systematic uncertainties on the determined number of fiducial neutrino interactions. The uncertainty components are added in quadrature such that the outer contour represents the total systematic uncertainty.

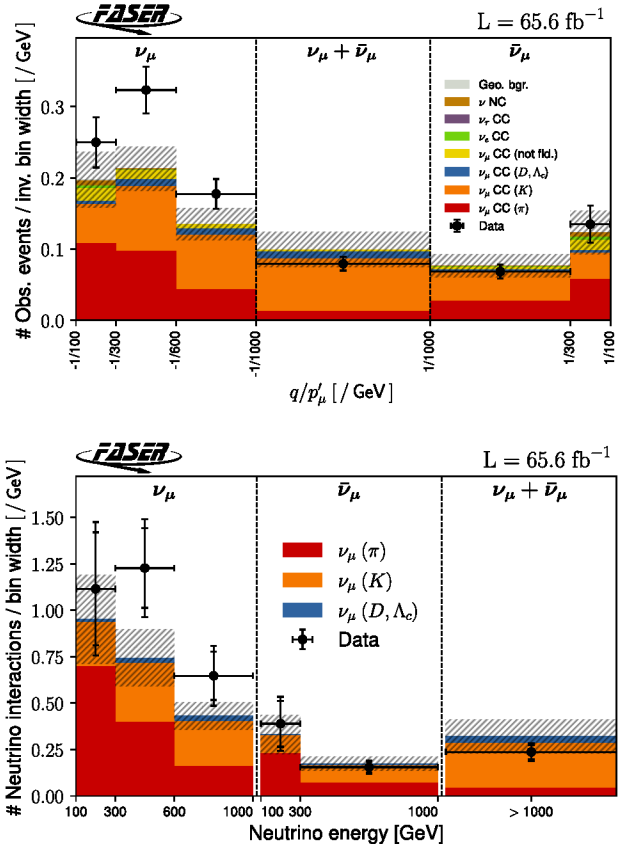

FIG. 2. (**Top**) The number of observed neutrino candidate events per inverse bin width (black markers) are compared to the expected number of CC, NC, and background contributions (histogram). (**Bottom**) The unfolded number of neutrino interactions per bin width (black markers) is compared to the expectation from the simulation (histograms). For the common high-energy bin we use a width of 868.2 GeV which contains 68.3 % of the simulated events. The inner error bars show the statistical uncertainty and the outer error bars the total uncertainty. The hatched area in both plots indicates the systematic uncertainty, whose dominant source stems from the neutrino flux predictions.

1 TeV than expected from simulation. More properties of the selected neutrino candidate events are summarized in appendix D.

Using the likelihood fit, defined in Eq. 2, and the efficiency and response matrix, detailed in appendix B, we determine $n_{\nu,\mathrm{fid}} = 1242.7 \pm 137.1$ CC muon neutrino interactions inside the fiducial volume. Fig. 2 (bottom panel) shows the unfolded number of neutrino interactions and compares them to the expectation from simulation.

The measured cross sections and neutrino fluxes are shown in Fig. 3. The dominant uncertainties for the cross sections measurement arise from the event statistics and the sizable uncertainty of the neutrino flux. We compare the measured collider neutrino cross sections with existing measurements from fixed-target neutrino experiments [38–49] at lower energies $E_\nu \lesssim 360\,\mathrm{GeV}$, with the measurement of the FASERν emulsion detector [8] at TeV energies, as well as measurements using astrophysical neutrinos observed at IceCube [50–52] at energies between 10 TeV and 10 PeV. We observe good agreement between the measured and expected cross section and fluxes. Additionally, Fig. 11 shows the simultaneous fit of the cross section and flux, both with and without constraints from the expected values from simulation.

The measured neutrino energy spectrum provides insight into their production mechanisms: muon neutrinos originating from pions generally have lower average energies than those from kaons or charmed mesons. This distinction is utilized to perform a χ^2 fit to the unfolded number of neutrino interactions. Fig. 4 shows the estimated number of neutrinos from pions versus kaons, as well as the expectation from various generators. We observe a larger pion-to-kaon ratio than expected, yielding a p-value of 5.9 % with SM expectations. This disfavors the explanations for the cosmic muon puzzle proposed in Refs. [53–56] that involve an enhanced forward strangeness production. More details on the template fit are given in appendix E.

Summary and Conclusions We present the first differential measurement of muon neutrino and antineutrino interactions probing neutrinos in the TeV energy range. The result was obtained analyzing $(65.6 \pm 1.4)\,\mathrm{fb}^{-1}$ of LHC pp collision data, recorded during 2022 and 2023. Neutrino candidates are selected using the active electronic components of the FASER detector. We observe in total 338.1 ± 21.0 neutrino events from CC ν_μ and $\bar{\nu}_\mu$ interactions in the fiducial volume, which agrees with the expectation within the uncertainties.

The measured muon momentum, q/p'_μ, is unfolded to the neutrino energy in six bins covering energies from

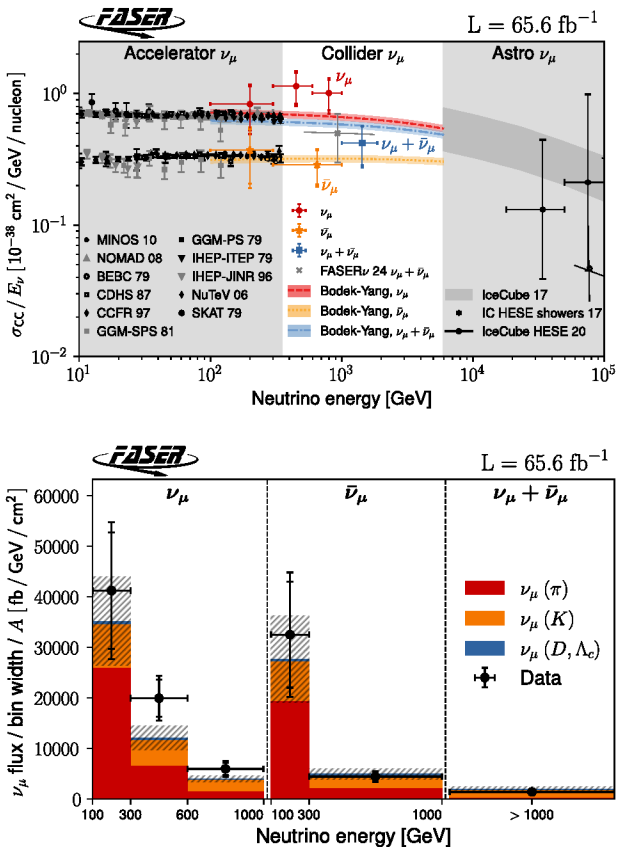

FIG. 3. (**Top**) Measured CC neutrino-nucleon cross sections divided by neutrino energy as a function of neutrino energy (colored markers), compared to predictions from the Bodek-Yang model (colored lines) and previous measurements from fixed-target and astrophysical sources (gray/black markers). The horizontal error bars show the widths of the energy bins. The common high-energy bin contains neutrinos and anti-neutrinos with a momentum larger than 1 TeV. This corresponds to the flux-weighted average cross section. It has a width of 868.2 GeV which contains 68.3 % of the simulated events. (**Bottom**) The measured neutrino flux divided by the energy and the cross sectional area of the fiducial volume (black markers) is compared to the expectation from the simulation (histograms). The inner error bars show the statistical uncertainty and the outer error bars the total uncertainty. The hatched area indicates the systematic uncertainties.

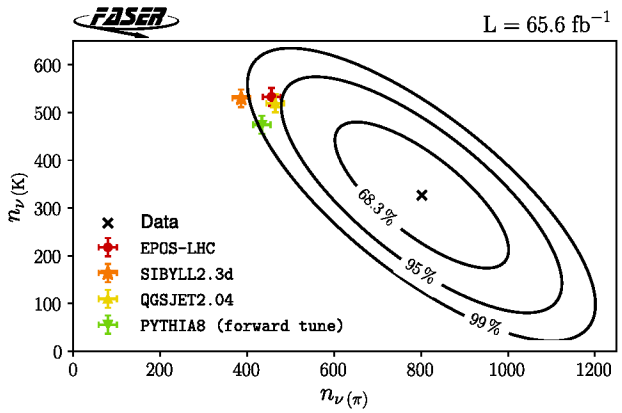

FIG. 4. Comparison of the number of neutrino interactions from pion and kaon decays with different MC generators. The 68.3 %, 95 % and 99 % confidence intervals, correspond to $\Delta\chi^2 = 2.3$, 5.99 and 9.21.

100 GeV to the TeV range. With this and the predicted neutrino and anti-neutrino flux the energy-dependent neutrino nucleon cross section is determined. Conversely, the predicted neutrino- and anti-neutrino-nucleon cross section is used to determine the differential muon neutrino flux. The contribution of neutrinos from pion and kaon decays is estimated using a template fit, finding a larger flux fraction for neutrinos from pions than kaons. These results together with the recent cross section measurement using the FASERν emulsion detector [8] represent the first studies of the neutrino-nucleon cross section and neutrino flux using collider neutrinos probing the TeV energy range, with wide ranging implications [9]. The presented results and the full experimental covariance matrix are available on `HEPData` [57].

Acknowledgments We thank CERN for the very successful operation of the LHC during 2022 and 2023. We thank the technical and administrative staff members at all FASER institutions for their contributions to the success of the FASER project. We thank the ATLAS Collaboration for providing us with accurate luminosity estimates for the used Run 3 LHC collision data. FASER gratefully acknowledges the donation of spare ATLAS SCT modules and spare LHCb calorimeter modules, without which the experiment would not have been possible. We also acknowledge the use of the ATLAS Collaboration software, Athena, on which FASER's offline software system is based [29] and the use of the ACTS tracking software framework [30]. Finally we thank the CERN STI group for providing detailed FLUKA simulations of the muon fluence along the LOS, which have been used in this analysis. This work was supported in part by Heising-Simons Foundation Grant Nos. 2018-1135, 2019-1179, and 2020-1840, Simons Foundation Grant No. 623683, U.S. National Science Foundation Grant Nos. PHY-2111427, PHY-2110929, and PHY-2110648, JSPS KAKENHI Grant Nos. 19H01909, 22H01233, 20K23373, 23H00103, 20H01919, and 21H00082, the joint research program of the Institute of Materials and Systems for Sustainability, ERC Consolidator Grant No. 101002690, Horizon 2020 Framework Programme Grant No. MUCCA CHIST-ERA-19-XAI-00, BMBF Grant No. 05H20PDRC1, DFG EXC 2121 Quantum Universe Grant No. 390833306, Royal Society Grant No. URF\R1\201519, U.K. Science and Technology Funding Councils Grant No. ST/T505870/1, the U.K. Science and Technology Funding Council, the National

Natural Science Foundation of China, Tsinghua University Initiative Scientific Research Program, and the Swiss National Science Foundation.

[1] **FASER** Collaboration, "Detecting and Studying High-Energy Collider Neutrinos with FASER at the LHC," *Eur. Phys. J. C* **80** (01, 2020) 61, arXiv:1908.02310 [hep-ex].

[2] J. L. Feng *et al.*, "The Forward Physics Facility at the High-Luminosity LHC," *J. Phys. G* **50** (2023) no. 3, 030501, arXiv:2203.05090 [hep-ex].

[3] **Particle Data Group** Collaboration, "Review of Particle Physics," *Phys. Rev. D* **110** (8, 2024) 030001.

[4] **IceCube** Collaboration, "Measurement of the multi-TeV neutrino cross section with IceCube using Earth absorption," *Nature* **551** (2017) 596–600, arXiv:1711.08119 [hep-ex].

[5] A. De Rujula and R. Ruckl, "Neutrino and muon physics in the collider mode of future accelerators," in *SSC Workshop: Superconducting Super Collider Fixed Target Physics*, pp. 571–596. 5, 1984.

[6] **FASER** Collaboration, "First Direct Observation of Collider Neutrinos with FASER at the LHC," *Phys. Rev. Lett.* **131** (2023) no. 3, 031801, arXiv:2303.14185 [hep-ex].

[7] **SND@LHC** Collaboration, "Observation of Collider Muon Neutrinos with the SND@LHC Experiment," *Phys. Rev. Lett.* **131** (2023) no. 3, 031802, arXiv:2305.09383 [hep-ex].

[8] **FASER** Collaboration, "First Measurement of ν_e and ν_μ Interaction Cross Sections at the LHC with FASER's Emulsion Detector," *Phys. Rev. Lett.* **133** (7, 2024) 021802, arXiv:2403.12520 [hep-ex].

[9] E. Worcester, "The Dawn of Collider Neutrino Physics," *APS Physics* **16** (2023) 113.

[10] **FASER** Collaboration, "The FASER Detector," *J. Instrum.* **19** (5, 2024) P05066, arXiv:2207.11427 [physics.ins-det].

[11] **FASER** Collaboration, "The trigger and data acquisition system of the FASER experiment," *JINST* **16** (2021) no. 12, P12028, arXiv:2110.15186 [physics.ins-det].

[12] **FASER** Collaboration, "The tracking detector of the FASER experiment," *Nucl. Instrum. Meth. A* **1034** (2022) 166825, arXiv:2112.01116 [physics.ins-det].

[13] A. Abdesselam *et al.*, "The barrel modules of the ATLAS semiconductor tracker," *Nucl. Instrum. Meth. A* **568** (2006) 642–671.

[14] **ATLAS** Collaboration, "Luminosity determination in pp collisions at $\sqrt{s} = 13$ TeV using the ATLAS detector at the LHC," *Eur. Phys. J. C* **83** (10, 2023) 982, arXiv:2212.09379 [hep-ex].

[15] **ATLAS** Collaboration, "Preliminary analysis of the luminosity calibration of the ATLAS 13.6 TeV data recorded in 2022," tech. rep., CERN, Geneva, 2023. https://cds.cern.ch/record/2853525.

[16] **ATLAS** Collaboration, "Preliminary analysis of the luminosity calibration for the ATLAS 13.6 TeV data recorded in 2023," tech. rep., CERN, Geneva, 2024. http://cds.cern.ch/record/2900949.

[17] F. Kling and L. J. Nevay, "Forward neutrino fluxes at the LHC," *Phys. Rev. D* **104** (2021) no. 11, 113008, arXiv:2105.08270 [hep-ph].

[18] **FASER** Collaboration, "Neutrino Rate Predictions for FASER," *Phys. Rev. D* **110** (7, 2024) 012009, arXiv:2402.13318 [hep-ex].

[19] T. Pierog *et al.*, "EPOS LHC: Test of collective hadronization with data measured at the CERN Large Hadron Collider," *Phys. Rev.* **C92** (2015) 034906, arXiv:1306.0121 [hep-ph].

[20] P. Nason, "A New method for combining NLO QCD with shower Monte Carlo algorithms," *JHEP* **11** (2004) 040, arXiv:hep-ph/0409146.

[21] S. Frixione *et al.*, "Matching NLO QCD computations with Parton Shower simulations: the POWHEG method," *JHEP* **11** (2007) 070, arXiv:0709.2092 [hep-ph].

[22] S. Alioli *et al.*, "A general framework for implementing NLO calculations in shower Monte Carlo programs: the POWHEG BOX," *JHEP* **06** (2010) 043, arXiv:1002.2581 [hep-ph].

[23] C. Bierlich *et al.*, "A comprehensive guide to the physics and usage of PYTHIA 8.3," *SciPost Phys. Codeb.* **2022** (2022) 8, arXiv:2203.11601 [hep-ph].

[24] L. Buonocore *et al.*, "Predictions for Neutrinos and New Physics from Forward Heavy Hadron Production at the LHC," *Eur. Phys. J. C, Particles and Fields* **84** (4, 2024) 363, arXiv:2309.12793 [hep-ph].

[25] C. Andreopoulos *et al.*, "The GENIE Neutrino Monte Carlo Generator," *Nucl. Instrum. Meth.* **A614** (2010) 87–104, arXiv:0905.2517 [hep-ph].

[26] C. Andreopoulos *et al.*, "The GENIE Neutrino Monte Carlo Generator: Physics and User Manual," arXiv:1510.05494 [hep-ph].

[27] **GENIE** Collaboration, "Neutrino-nucleon cross-section model tuning in GENIE v3," *Phys. Rev. D* **104** (2021) no. 7, 072009, arXiv:2104.09179 [hep-ph].

[28] **GEANT4** Collaboration, "GEANT4–a simulation toolkit," *Nucl. Instrum. Meth. A* **506** (2003) 250–303.

[29] **ATLAS** Collaboration, "The ATLAS Collaboration Software and Firmware." ATL-SOFT-PUB-2021-001, 2021. https://cds.cern.ch/record/2767187.

[30] X. Ai *et al.*, "A Common Tracking Software Project," *Comput. Softw. Big Sci.* **6** (2022) no. 1, 8, arXiv:2106.13593 [physics.ins-det].

[31] H. Dembinski *et al.*, "scikit-hep/iminuit,". https://doi.org/10.5281/zenodo.3949207.

[32] A. Bodek *et al.*, "Modeling deep inelastic cross-sections in the few GeV region," *Nucl. Phys. B Proc. Suppl.* **112** (2002) 70–76, arXiv:hep-ex/0203009.

[33] A. Bodek *et al.*, "Improved low Q**2 model for neutrino and electron nucleon cross sections in few GeV region," *Nucl. Phys. B Proc. Suppl.* **139** (2005) 113–118, arXiv:hep-ph/0411202.

[34] A. Bodek *et al.*, "Axial and Vector Structure Functions for Electron- and Neutrino- Nucleon Scattering Cross Sections at all Q^2 using Effective Leading order Parton Distribution Functions," arXiv:1011.6592 [hep-ph].

[35] A. Candido *et al.*, "Neutrino Structure Functions from GeV to EeV Energies," *JHEP* **05** (2023) 149, arXiv:2302.08527 [hep-ph].

[36] Y. S. Jeong and M. H. Reno, "Neutrino cross sections: Interface of shallow- and deep-inelastic scattering for collider neutrinos," *Phys. Rev. D* **108** (2023) no. 11,

113010, arXiv:2307.09241 [hep-ph].

[37] **CMS** Collaboration, "Strategies and performance of the CMS silicon tracker alignment during LHC Run 2," *Nucl. Instrum. Meth. A* **1037** (2022) 166795, arXiv:2111.08757 [physics.ins-det].

[38] J. G. H. de Groot *et al.*, "Inclusive Interactions of High-Energy Neutrinos and anti-neutrinos in Iron," *Z. Phys. C* **1** (1979) 143.

[39] D. C. Colley *et al.*, "Cross-sections for Charged Current Neutrino and Anti-neutrino Interactions in the Energy Range 10-GeV to 50-GeV," *Z. Phys. C* **2** (1979) 187.

[40] W. G. Seligman, *A Next-to-Leading Order QCD Analysis of Neutrino - Iron Structure Functions at the Tevatron*. PhD thesis, Nevis Labs, Columbia U., 1997.

[41] J. P. Berge *et al.*, "Total Neutrino and Anti-neutrino Charged Current Cross-section Measurements in 100-GeV, 160-GeV and 200-GeV Narrow Band Beams," *Z. Phys. C* **35** (1987) 443.

[42] **Gargamelle Neutrino Propane, Aachen-Brussels-CERN-Ecole Poly-Orsay-Padua** Collaboration, "Total Cross-section for Neutrino Charged Current Interactions at 3-GeV and 9-GeV," *Phys. Lett. B* **84** (1979) 281–284.

[43] **Gargamelle SPS** Collaboration, "Total Cross-sections and Nucleon Structure Functions in the Gargamelle SPS Neutrino / Anti-neutrino Experiment," *Phys. Lett. B* **104** (1981) 235–238.

[44] A. I. Mukhin *et al.*, "Energy Dependence of Total Cross-sections for Neutrino and Anti-neutrino Interactions at Energies Below 35-GeV," *Sov. J. Nucl. Phys.* **30** (1979) 528.

[45] V. B. Anikeev *et al.*, "Total cross-section measurements for muon-neutrino, anti-muon-neutrino interactions in 3-GeV - 30-GeV energy range with IHEP-JINR neutrino detector," *Z. Phys. C* **70** (1996) 39–46.

[46] **MINOS** Collaboration, "Neutrino and Antineutrino Inclusive Charged-current Cross Section Measurements with the MINOS Near Detector," *Phys. Rev. D* **81** (2010) 072002, arXiv:0910.2201 [hep-ex].

[47] **NOMAD** Collaboration, "A Precise measurement of the muon neutrino-nucleon inclusive charged current cross-section off an isoscalar target in the energy range 2.5 < E(nu) < 40-GeV by NOMAD," *Phys. Lett. B* **660** (2008) 19–25, arXiv:0711.1183 [hep-ex].

[48] **NuTeV** Collaboration, "Precise measurement of neutrino and anti-neutrino differential cross sections," *Phys. Rev. D* **74** (2006) 012008, arXiv:hep-ex/0509010.

[49] D. Baranov *et al.*, "Measurement of the ν_μ-N total cross section at 2–30 GeV in a SKAT neutrino experiment," *Phys. Lett. B* **81** (1979) no. 2, 255–257.

[50] **IceCube** Collaboration, "Measurement of the multi-TeV neutrino cross section with IceCube using Earth absorption," *Nature* **551** (2017) 596–600, arXiv:1711.08119 [hep-ex].

[51] M. Bustamante and A. Connolly, "Extracting the Energy-Dependent Neutrino-Nucleon Cross Section above 10 TeV Using IceCube Showers," *Phys. Rev. Lett.* **122** (2019) no. 4, 041101, arXiv:1711.11043 [astro-ph.HE].

[52] **IceCube** Collaboration, "Measurement of the high-energy all-flavor neutrino-nucleon cross section with IceCube," *Phys. Rev. D* **104** (Jul, 2021) 022001, arXiv:2011.03560 [hep-ex].

[53] H. P. Dembinski *et al.*, "Report on Tests and Measurements of Hadronic Interaction Properties with Air Showers," *EPJ Web of Conferences* **210** (2019) 02004, arXiv:1902.08124 [astro-ph.HE].

[54] J. Albrecht *et al.*, "The Muon Puzzle in Cosmic-Ray Induced Air Showers and Its Connection to the Large Hadron Collider," *Astrophysics and Space Science* **367** (3, 2022) 27, arXiv:2105.06148 [astro-ph.HE].

[55] L. A. Anchordoqui *et al.*, "An Explanation of the Muon Puzzle of Ultrahigh-Energy Cosmic Rays and the Role of the Forward Physics Facility for Model Improvement," *Journal of High Energy Astrophysics* **34** (6, 2022) 19–32, arXiv:2202.03095 [hep-ph].

[56] **EAS-MSU, IceCube, KASCADE-Grande, NEVOD-DECOR, Pierre Auger, SUGAR, Telescope Array, Yakutsk EAS Array** Collaboration, D. Soldin, "Update on the Combined Analysis of Muon Measurements from Nine Air Shower Experiments," *PoS* **ICRC2021** (2021) 349, arXiv:2108.08341 [astro-ph.HE].

[57] **FASER** Collaboration, "First Measurement of the Muon Neutrino Interaction Cross Section and Flux as a Function of Energy at the LHC with FASER." HEPData (collection), 2025. https://doi.org/10.17182/hepdata.156838.v1.

[58] F. Riehn *et al.*, "Hadronic interaction model Sibyll 2.3d and extensive air showers," *Phys. Rev. D* **102** (2020) no. 6, 063002, arXiv:1912.03300 [hep-ph].

[59] S. Ostapchenko, "Monte Carlo treatment of hadronic interactions in enhanced Pomeron scheme: I. QGSJET-II model," *Phys. Rev.* **D83** (2011) 014018, arXiv:1010.1869 [hep-ph].

[60] M. Fieg *et al.*, "Tuning pythia for forward physics experiments," *Phys. Rev. D* **109** (2024) no. 1, 016010, arXiv:2309.08604 [hep-ph].

[61] D. Mancusi *et al.*, "Improving the description of proton-induced one-nucleon removal in intranuclear-cascade models," *Phys. Rev. C* **91** (2015) no. 3, 034602, arXiv:1411.4562 [nucl-th].

[62] E. Mendoza *et al.*, "New Standard Evaluated Neutron Cross Section Libraries for the GEANT4 Code and First Verification," *IEEE Transactions on Nuclear Science* **61** (2014) 2357–2364.

[63] E. Mendoza *et al.*, "Update of the Evaluated Neutron Cross Section Libraries for the Geant4 Code," tech. rep., International Atomic Energy Agency (IAEA), 2018.

[64] A. J. M. Plompen *et al.*, "The Joint Evaluated Fission and Fusion Nuclear Data Library, JEFF-3.3," *Eur. Phys. J. A* **56** (2020) no. 7, 181.

[65] D. A. Brown *et al.*, "ENDF/B-VIII.0: The 8th Major Release of the Nuclear Reaction Data Library with CIELO-project Cross Sections, New Standards and Thermal Scattering Data," *Nuclear Data Sheets* **148** (2018) 1–142.

APPENDIX

Appendix A: Geometric Muon Background

The distribution of the transverse distance from the detector axis of the track when extrapolated to the VetoNu scintillator, r_{VetoNu}, and the track momentum, p_μ, in Fig. 5 (left) shows a clear separation between signal events (black dashed box), and background events with momenta $\lesssim 20\,\mathrm{GeV}$. Events with a momentum between 20 GeV and 100 GeV are consistent with neutrino simulation.

Fig. 5 (right) shows the extrapolation of the geometric muon background from the sideband into the signal region. The neutrino expectation is subtracted from the data and fitted with an exponential function. Systematic variations in the extrapolation fit were also tested, but as the resulting change in the background predictions were within the data statistical uncertainties no additional uncertainty was applied.

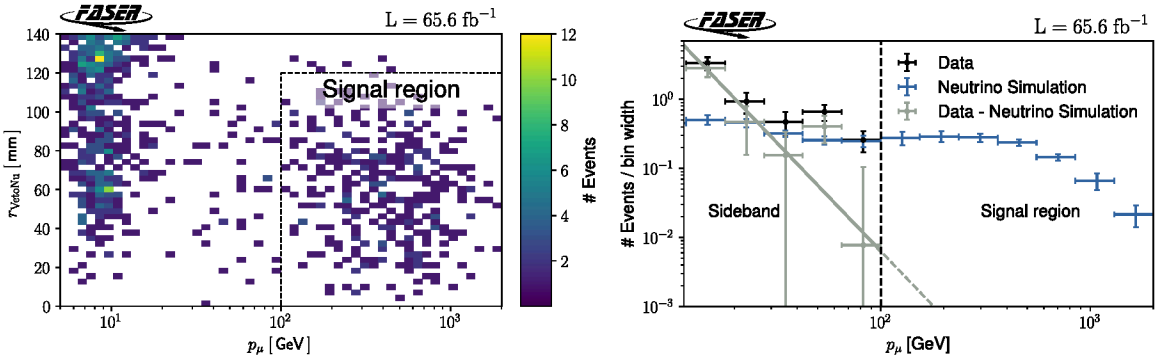

FIG. 5. (**Left**) The distribution of the extrapolated, transverse track position at the VetoNu scintillator station, r_{VetoNu}, and momentum, p_μ. The black box shows the signal region. (**Right**) The fit to the geometric muon background in the region $p_\mu < 100\,\mathrm{GeV}$ is shown for negatively charged tracks. The simulated neutrino prediction (blue) is subtracted from the data (black), and the result (gray) is fitted and extrapolated to $p_\mu > 100\,\mathrm{GeV}$.

Appendix B: Response Matrix and Efficiency

Fig. 6 shows the response matrix relating the calibrated, reconstructed muon momentum q/p'_μ to the neutrino energy $-L/E_\nu$, expressed as a conditional probability. Using the calibrated muon momentum, $p'_\mu = p_\mu/0.8$, results in a more diagonal response matrix, and therefore smaller uncertainties on the unfolded number of neutrino interactions.

Table II shows the detector acceptance and reconstruction efficiency. The acceptance is the fraction of neutrino interactions in the fiducial volume where the produced muon has a momentum larger 100 GeV and goes through the active transverse area of the whole detector at truth level. The transverse momentum of the muon produced in the neutrino interaction is particularly relevant for low-energy neutrinos, resulting in smaller acceptances in the corresponding bins. In addition, negatively charged muons typically get a smaller fraction of the neutrino energy, resulting in an asymmetry between neutrinos and anti-neutrinos. The reconstruction efficiency is the fraction of these events which pass the event selection. The inefficiency is dominated by the angular and the VetoNu charge cut. The efficiency used in Eq. 1 is the product of acceptance and reconstruction efficiency.

TABLE II. Acceptance, reconstruction efficiency, and total efficiency in percent in bins of the neutrino energy, $-L/E_\nu$. The uncertainties describe the modeling of the neutrino flux and interactions, the change of the LOS, and the detector response.

$-L/E_\nu$ $\left[\mathrm{GeV}^{-1}\right]$	$\left[\frac{-1}{100}, \frac{-1}{300}\right]$	$\left[\frac{-1}{300}, \frac{-1}{600}\right]$	$\left[\frac{-1}{600}, \frac{-1}{1000}\right]$	$\left[\frac{-1}{1000}, \frac{1}{1000}\right]$	$\left[\frac{1}{1000}, \frac{1}{300}\right]$	$\left[\frac{1}{300}, \frac{1}{100}\right]$	Total
Acceptance α [%]	16.7± 0.6	30.0± 1.2	38.8± 2.6	46.6± 3.0	47.5± 1.9	27.8± 2.5	35.3± 2.0
Reco. efficiency $\epsilon_{\mathrm{reco.}}$ [%]	80.8± 7.2	79.0± 4.9	79.3± 5.0	78.8± 5.5	84.4± 4.7	84.5± 6.9	80.3± 4.5
Efficiency $\epsilon = \alpha \cdot \epsilon_{\mathrm{reco}}$ [%]	13.5± 1.2	23.7± 1.7	30.8± 2.6	36.8± 3.0	40.1± 3.1	23.5± 2.4	28.3± 1.9

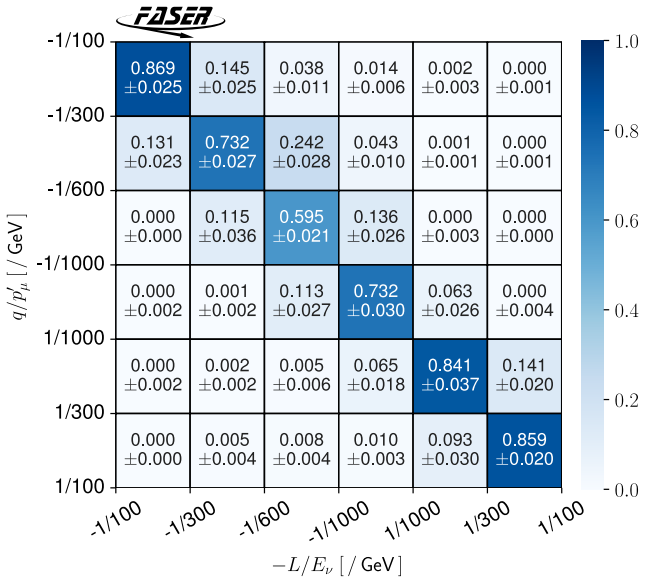

FIG. 6. The response matrix relating the reconstructed, calibrated muon momentum q/p'_μ to the neutrino energy $-L/E_\nu$, expressed as a conditional probability. The off-diagonal elements are dominated by the fluctuations in the fraction of the neutrino energy that the muon takes in the interaction. The uncertainties reflect the quadratic sum of statistical and systematic uncertainties and are dominated by the modeling of the neutrino interactions (these uncertainties are about 2.5 times larger than detector related uncertainties, such as alignment).

Appendix C: Flux and neutrino interaction modeling uncertainties

The primary source of the neutrino flux uncertainty originates from the modeling of the forward hadron rate. To estimate this uncertainty for light hadron production, we follow Ref. [18] and consider the range of predictions from `EPOS-LHC`, `Sibyll 2.3d` [58], `QGSJET 2.04` [59], and the forward physics tune of `PYTHIA` [60]. For heavy hadron production we follow Ref. [24] and vary the factorization and renormalization scales by a factor of 2 around their nominal value.

The neutrino interactions with the detector material are simulated with `GENIE 3.04.0` [25–27]. To estimate the uncertainty from the modeling of final state interactions and intranuclear hadron transport, two different tunes are applied using the default `INTRANUKE hA` effective intranuclear rescattering model and the `INCL++` implementation of the Liège intranuclear model [61]. The passage of the particles produced in neutrino interactions through the detector is simulated with `GEANT4`. To estimate the uncertainty from hadron transport [62, 63], we study the `FTFP_INCLXX`, `FTF_BIC`, and `FTFP_BERT_HP` physics lists together with the `G4NDL`, `JEFF-3.3` [64] and `ENDF/B-VIII.0` [65] neutron data libraries.

Appendix D: Comparison of signal and background distributions

We compare the distribution of the signal events, with simulation and background-like events. In the following signal refers to muons produced in a neutrino interaction in the tungsten target, and background muons refers to muons from the decay of particles produced at the ATLAS IP. For the background, we select events which pass the event selection but have a reduced charge larger than 30 pC in both layers of the VetoNu scintillator: (i) Background events have usually only a single muon traversing the IFT, which creates one hit in each wafer, resulting in a total of six hits. In contrast, the neutrino interactions can produce an electromagnetic and hadronic shower which may hit the IFT, resulting in a large number of hits. (ii) Muons from the decay of particles produced at the ATLAS IP are only slightly deflected by the LHC magnets (otherwise they miss the FASER detector), resulting in small angles with respect to the LOS. In contrast, muons produced in a neutrino interaction in the tungsten target can have much larger angles. (iii) Muons from background and signal events have slightly different q/p_μ distributions. As shown in

Fig. 7, for these distributions signal events agree with simulation, but are very distinct from background-like events.

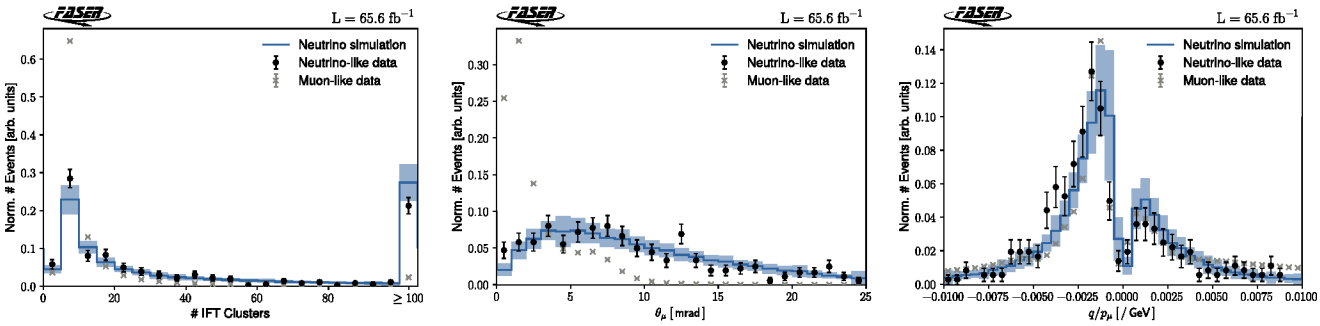

FIG. 7. Number of clusters in the IFT (**left**), track polar angle θ_μ (**center**) at the first station of the tracking spectrometer, and the ratio of the muon unit charge and momentum q/p_μ (**right**) for signal events (black markers), muon-like events (gray markers), and simulation (blue histogram). The muon-like data pass the same event-selection as signal events, but have a reduced charge larger than 30 pC in both layers of the VetoNu scintillator station. The uncertainty of the simulated events describes the modeling of the neutrino flux and neutrino interactions, the change of the LOS, the detector response, and the luminosity and mass uncertainties.

Appendix E: Fit of neutrinos from pions and kaons

The unfolded number of neutrino interactions is analyzed to determine the fractions of neutrinos originating from pion and kaon decays. The expected number of neutrino interactions in bin i of the unfolded neutrino energy can be calculated as $\nu_\nu^i = \sum_k f_{ik}\eta_k$, where η_k denotes the total number of neutrino interactions from production mode k, and f_{ik} represents the fraction of these neutrino interactions in bin i, obtained from simulation. Since the expected contribution from charmed hadrons is small and the shapes of charm and kaon contributions are similar, we fix it to the expected value within uncertainties. To determine the number of neutrino interactions, we perform a χ^2 fit with

$$\chi^2 = (\vec{\nu} - \vec{n})^T \, \mathrm{Cov}^{-1} \, (\vec{\nu} - \vec{n}) + \mathcal{G} \, , \tag{E1}$$

where $\vec{n}$ and Cov represent the number and covariance matrix of neutrino interactions obtained from the likelihood fit in Eq. 2. Systematic uncertainties on the fractions f_{ik} are implemented with nuisance parameters and are constrained with Gaussian priors $\mathcal{G}$, but correlations between different templates are not taken into account. They are dominated by the shape uncertainties from different generators.

SUPPLEMENTAL MATERIAL

I. REDUCED VETONU CHARGE

The left panel in Fig. 8 illustrates how a muon and neutrino deposit charge in the vetoNu and veto scintillators. The right panel shows the simulated waveforms in these scintillator stations for a typical muon and neutrino event and explains the calculation of the reduced vetoNu charge.

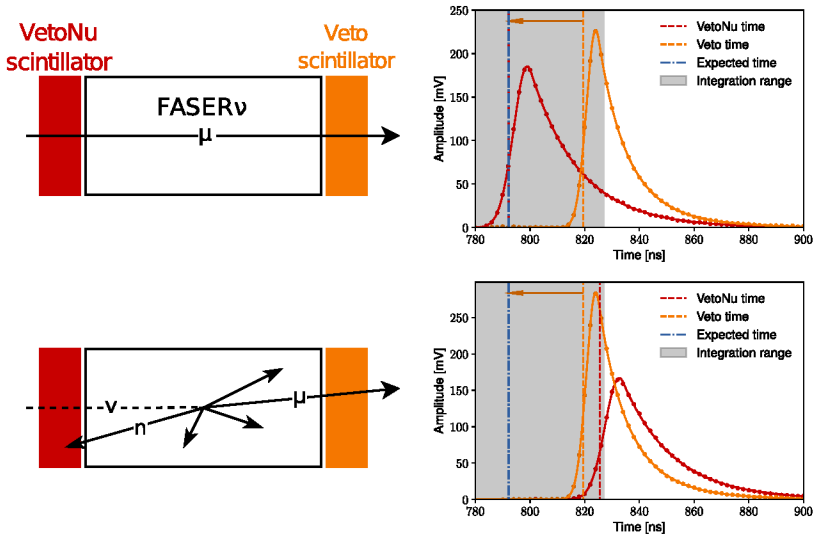

FIG. 8. (**Left**) Depiction of a muon (top) and a neutrino (bottom) traversing the FASERν detector and depositing charge in the vetoNu (red) and veto (orange) scintillator stations. (**Right**) Waveforms of the vetoNu and veto charge. The red and orange lines show the time where the rising edge of the amplitude is 40 % of the maximum value. The blue line shows the expected time, which is calculated from the measured local veto time and the average time-of-flight of muons. To cover also the tail of the waveforms a constant 35 ns offset is added to the expected time, which is indicated by the gray area. The reduced charge is defined as the measured charge in each of the two vetoNu scintillators integrated over this time window.

II. SIMULATED NEUTRINO FLUX AND EFFECTIVE CROSS SECTION

Table III shows the simulated neutrino flux and effective cross section in bins of the neutrino energy. The uncertainty of the simulated flux is dominated by the modeling from different generators. The effective cross section is the flux-weighted average and depends on the modeling within each energy bin. A systematic uncertainty is applied to account for the difference between the used generators. Additionally, a 6 % uncertainty is applied to account for the difference between the Bodek-Yang model [32–34] employed in `GENIE` and more recent cross section models [35, 36].

TABLE III. Simulated neutrino flux and effective cross section

$-L/E_\nu$ $\left[\mathrm{GeV}^{-1}\right]$	$\left[\frac{-1}{100}, \frac{-1}{300}\right]$	$\left[\frac{-1}{300}, \frac{-1}{600}\right]$	$\left[\frac{-1}{600}, \frac{-1}{1000}\right]$	$\left[\frac{-1}{1000}, \frac{1}{1000}\right]$	$\left[\frac{1}{1000}, \frac{1}{300}\right]$	$\left[\frac{1}{300}, \frac{1}{100}\right]$
$\phi_{\mathrm{Sim.}}$ $[10^6 \mathrm{fb\,cm}^{-2}]$	7.0± 1.8	3.6± 0.7	1.6± 0.3	1.7± 0.5	3.5± 0.8	5.5± 1.7
$\sigma_{\mathrm{sim.}}$ $[10^{-38}$ cm^2 / nucleon]	128.5± 7.9	292.2±17.6	514.6±31.3	799.3±68.1	166.3±10.5	56.8± 3.4

III. COMPARISON OF EPOS-LHC+POWHEG+PYTHIA8 AND DPMJET

Fig. 9 compares the unfolded number of neutrino interactions with the expectation from EPOS-LHC, POWHEG, and PYTHIA8 and with the expectation from DPMJET 3.2019.1.

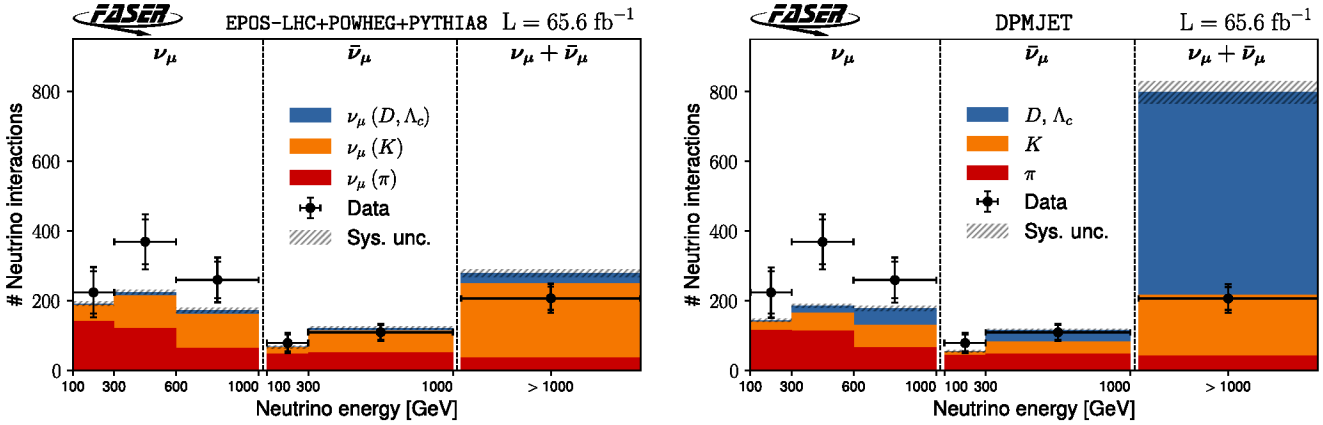

FIG. 9. The observed number of neutrino interactions (black markers) is compared to the expectation from EPOS-LHC for neutrinos from the decay of pions and kaons and POWHEG and PYTHIA 8.3 for the decay of charmed hadrons (**left**) and DPMJET 3.2019.1 (**right**). The inner error bars show the statistical uncertainty and the outer error bars the total uncertainty. The hatched area in both plots indicates the systematic uncertainty without the neutrino flux modeling uncertainty (which was previously calculated from the difference of various generators).

IV. PRE- AND POST-FIT DISTRIBUTIONS FOR THE PION/KAON FIT

Fig. 10 compares the unfolded number of neutrino interactions with the pre- and post-fit expectations.

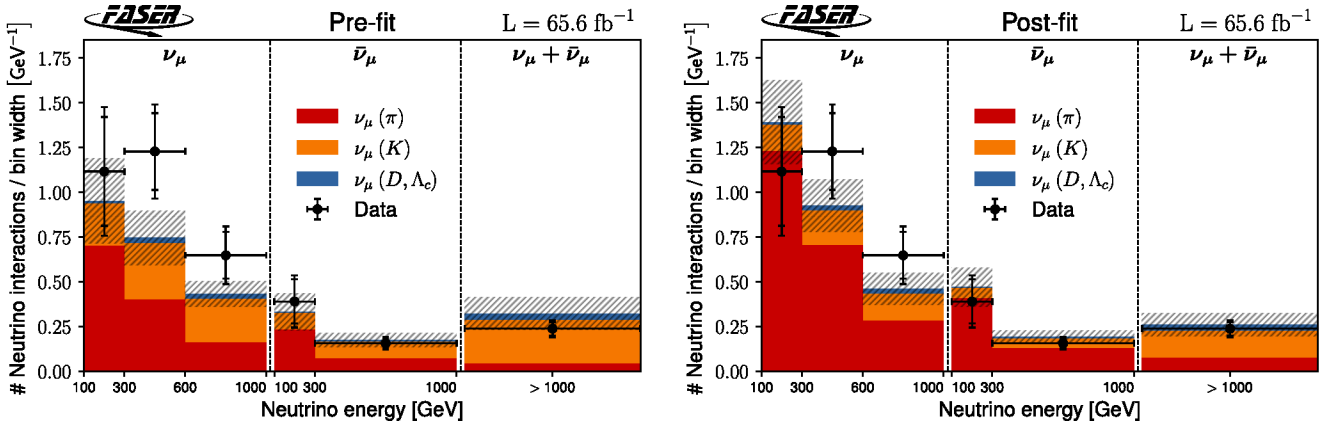

FIG. 10. The observed number of neutrino interactions (black markers) is compared to the pre-fit expectation with a total of 456.0 ± 70.6 neutrinos from pion decays and 532.9 ± 59.3 neutrinos from kaon decays (**left**) and the post-fit expectation with a total of 802.0 ± 131.8 neutrinos from pion decays and 326.6 ± 100.9 neutrinos from kaon decays (**right**).

V. SIMULTANEOUS FIT

To simultaneously measure the flux, ϕ^k, and cross section, σ^k_{CC}, in each $-L/E_\nu$-bin k, we minimize the following χ^2 function:

$$\chi^2_k = \frac{\left(\phi^k \cdot \sigma^k_{\mathrm{CC}} \cdot \rho_T \cdot L - n^k_\nu\right)^2}{\left(\delta^k_n\right)^2}, \tag{1}$$

with n^k_ν and δ^k_n denoting the unfolded number and uncertainty of neutrino interactions in bin k. We also perform a constrained fit using the expected flux and cross section values from simulation

$$\chi^2_{k,\ \mathrm{const.}} = \frac{\left(\phi^k \cdot \sigma^k_{\mathrm{CC}} \cdot \rho_T \cdot L - n^k_\nu\right)^2}{\left(\delta^k_n\right)^2} + \frac{\left(\phi^k - \phi^k_{\mathrm{sim.}}\right)^2}{\left(\delta^k_{\phi,\ \mathrm{sim.}}\right)^2} + \frac{\left(\sigma^k_{\mathrm{CC}} - \sigma^k_{\mathrm{sim.}}\right)^2}{\left(\delta^k_{\sigma,\ \mathrm{sim.}}\right)^2} \tag{2}$$

Fig. 11 compares the measured flux and cross section described above with the results of the simultaneous fits.

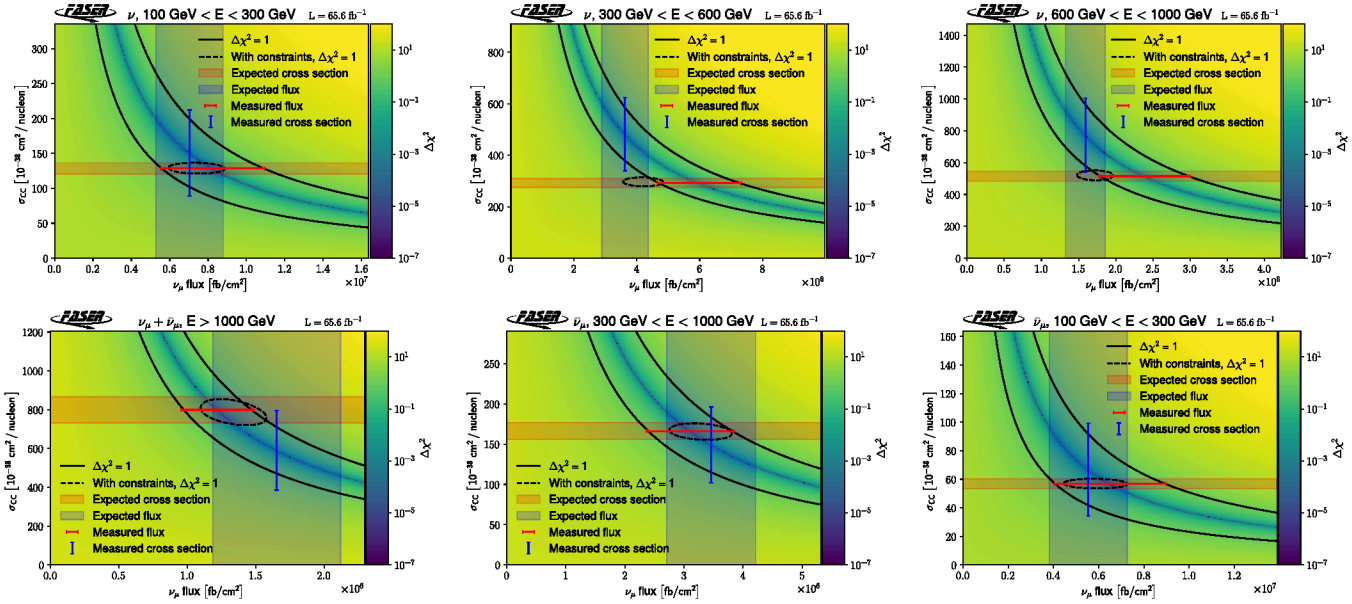

FIG. 11. The contour plots of cross section versus flux for each $-L/E_\nu$ bin. The blue bands and error bars show the expected flux and the corresponding measured cross section. And the red bands and error bars show the expected cross section and the corresponding measured flux. The black, dashed ellipses show the best fit result when constraining the cross section and flux with the expected values.